

One-Step Preparation of Biocompatible Gold Nanoplates with Controlled Thickness and Adjustable Optical Properties for Plasmon-Based Applications

Sunjie Ye, Simon D. Connell, James R. McLaughlan, Lucien Roach, Zabeada Aslam, Navadecho Chankhunthod, Andy P. Brown, Rik Brydson, Richard J. Bushby, Kevin Critchley, P. Louise Coletta, Alexander F. Markham, and Stephen D. Evans*


The ability to synthesize plasmonic nanomaterials with well-defined structures and tailorable size is crucial for exploring their potential applications. Gold nanoplates (AuNPLs) exhibit appealing structural and optical properties, yet their applications are limited by difficulties in thickness control. Other challenges include a narrow range of tunability in size and surface plasmon resonance, combined with a synthesis conventionally involving cytotoxic cetyltrimethylammonium (CTA) halide surfactant. Here, a one-step, high-yield synthesis of single-crystalline AuNPLs is developed, based on the combined use of two structure-directing agents, methyl orange and FeBr_3 , which undergo preferential adsorption onto different crystalline facets of gold. The obtained AuNPLs feature high shape homogeneity that enables mesoscopic self-assembly, broad-range tunability of dimensions (controlled thickness from ≈ 7 to ≈ 20 nm, accompanied by modulation of the edge length from ≈ 150 nm to ≈ 2 μm) and plasmonic properties. These merits, coupled with a preparation free of CTA-halide surfactants, have facilitated the exploration of various uses, especially in bio-related areas. For example, they are demonstrated as biocompatible photothermal agents for cell ablation in NIR I and NIR II windows. This work paves the way to the innovative fabrication of anisotropic plasmonic nanomaterials with desired attributes for wide-ranging practical applications.

1. Introduction

Colloidal plasmonic nanomaterials hold great potential across a broad array of applications. These include plasmonic-based diagnosis and therapy, surface-enhanced Raman scattering (SERS), plasmon-enhanced photocatalysis amongst others.^[1–3] The performance of these nanomaterials depends on their plasmonic properties, which are essentially dictated by shape, size, and composition.^[4,5] It is therefore important to develop reliable and robust synthesis methods that allow precise control over architectural parameters. Gold nanoplates (AuNPLs) are quasi-2D nanomaterials that exhibit a number of unique structural and optical properties, including: 1) corners and edges which provide pronounced electric-field enhancement^[6]; 2) atomically flat surfaces, which render them applicable for developing metasurfaces and for fabricating plasmon-based optical devices^[7]; 3) multiple surface plasmon resonance

Dr. S. Ye, Prof. S. D. Connell, Dr. L. Roach, Prof. R. J. Bushby, Prof. K. Critchley, Prof. S. D. Evans
School of Physics and Astronomy
University of Leeds
Leeds LS2 9JT, UK
E-mail: s.d.evans@leeds.ac.uk

Dr. S. Ye, Dr. P. L. Coletta, Prof. A. F. Markham
Leeds Institute of Medical Research
St James's University Hospital
University of Leeds
Leeds LS9 7TF, UK

 The ORCID identification number(s) for the author(s) of this article can be found under <https://doi.org/10.1002/adfm.202003512>.

© 2020 The Authors. Published by WILEY-VCH Verlag GmbH & Co. KGaA, Weinheim. This is an open access article under the terms of the Creative Commons Attribution License, which permits use, distribution and reproduction in any medium, provided the original work is properly cited.

DOI: 10.1002/adfm.202003512

Dr. S. Ye, Prof. S. D. Connell, Dr. L. Roach, Dr. Z. Aslam, N. Chankhunthod, Prof. A. P. Brown, Prof. R. Brydson, Prof. K. Critchley, Prof. S. D. Evans
Bragg Centre for Materials Research
University of Leeds
Leeds LS2 9JT, UK

Dr. J. R. McLaughlan
School of Electronic and Electrical Engineering
University of Leeds
Leeds LS2 9JT, UK

Dr. Z. Aslam, N. Chankhunthod, Prof. A. P. Brown, Prof. R. Brydson
School of Chemical and Process Engineering
University of Leeds
Leeds LS2 9JT, UK

Prof. R. J. Bushby
School of Chemistry
University of Leeds
Leeds LS2 9JT, UK

(SPR) modes, for example, in-plane dipolar and quadrupolar plasmon modes^[8–10]; 4) high sensitivity of localized SPR that can be harnessed for plasmonic sensing^[5,11,12]; 5) multivalent interactions at bio-interfaces due to a planar geometry, favorable for applications which need high-level surface interactions at a small scale^[13]; and 6) superior catalytic performance to that of isotropic counterparts.^[14]

The past decade has seen a series of significant advances in the synthesis of AuNPLs, these have facilitated the discovery of novel properties and phenomena. Millstone et al. successfully produced AuNPLs with a thickness of 75 nm and an average edge length of 144 nm.^[9] The high shape purity of the AuNPLs obtained led to the identification of the quadrupolar plasmon resonance, which had been previously unobservable in solution due to impurities and inhomogeneity of synthesized nanoplates. The Liz-Marzán group reported the synthesis of triangular AuNPLs with a thickness of ≈ 30 nm and edge lengths of 50–150 nm.^[3] The as-prepared AuNPLs displayed a remarkably improved monodispersity (down to 3% standard deviation) and a high shape yield (>50%), that was increased to >95%, following a simple purification. Such a high monodispersity contributed to the formation of extended self-assembled monolayers of AuNPLs, which displayed superior performance as SERS substrates. Zhang's group developed a high-yield seedless synthesis of monodispersed triangular AuNPLs, which had a high morphological yield (>90%), a thickness of ≈ 15 nm, and a tunable edge length (≈ 45 –120 nm).^[15] Oxidative etching of iodide ions was found to be critical in achieving the high yield and uniform morphology by this synthesis route. These methods conventionally rely on the adoption of cetyltrimethylammonium (CTA) halides (e.g., bromide, chloride) as structure-directing capping agents. However, these CTA halide-based surfactants are known to cause limited reproducibility in syntheses^[16,17] and high toxicities in bio-related applications.^[18,19] To address these issues, the Yin group developed a synthesis of biocompatible AuNPLs (thickness: ≈ 12 nm) with excellent reproducibility and high yield using polyvinylpyrrolidone (PVP) and H₂O₂, and demonstrated improved biocompatibility of these AuNPLs.^[20] Pelaz et al. reported a preparation of biocompatible AuNPLs with a thickness of 9 nm and tunable edge length of 100–179 nm, based on reduction of chloroauric acid (HAuCl₄) by sodium thiosulfate (Na₂S₂O₃).^[21] In these two cases, the easy surface functionalization of AuNPLs was achieved for potential bio-applications.

Despite the significant progress in the fabrication of AuNPLs, thickness control remains in its infancy. This limits the synthetically tailorable range of aspect ratios and consequently confines the adjustability of the in-plane SPR to a narrow window of wavelength. To our knowledge, there have only been two examples regarding thickness adjustment of colloidal AuNPLs, both of which involved overgrowth of previously synthesized AuNPLs to confer different thicknesses. For example, Kim et al. presented the high-yield synthesis of triangular AuNPLs with controllable structural parameters.^[22] In that work, AuNPLs were first prepared via a multi-step CTAB-mediated seeded growth, and then subjected to further isotropic overgrowth to achieve enlargement in three dimensions for providing tailorable edge lengths and thicknesses. Qin et al. demonstrated thickness control of hexagonal AuNPLs,^[5] via a multiple-step

approach. The protocol sequentially included 1) synthesis and sedimentation separation to obtain triangular AuNPLs with high shape purity, 2) rounding of the triangular AuNPLs via atom migration, and 3) nanocrystal overgrowth on the rounded AuNPLs. As a result, the SPR of the AuNPLs was shifted from the near-infrared to the visible region. A recent alternative approach to the thickness control of AuNPLs involved one-step synthesis of truncated hexagonal AuNPLs deposited on graphene multilayers.^[23] The lateral size of these AuNPLs could be varied from ≈ 27 nm to ≈ 4.9 μ m, and the thickness could be controlled between ≈ 13 and ≈ 46 nm. To date, thickness-controlled preparation of unsupported AuNPLs in a single step has not been realized.

Here, we present a conceptually novel method that enables one-step synthesis of biocompatible colloidal AuNPLs of controlled thickness. The key to our synthesis lies in the combined use of methyl orange (MO) and bromide ions to direct nanocrystal growth. The resulting AuNPLs meet the criteria of high shape purity, broad-range tunability of dimensions and hence plasmonic properties. These features allow us to achieve large area, ordered self-assembly, and explore diverse plasmonic properties of AuNPLs. As the synthesis method is free of halide-containing surfactants, as well as providing adjustable dipolar and quadrupolar plasmon resonances, our AuNPLs have demonstrated low cytotoxicities and the ability to induce photothermal cell ablation in both the NIR I and NIR II optical windows.

2. Results and Discussion

2.1. One-Step Synthesis of AuNPLs

Challenges in the production of anisotropic metal nanostructures arise from the tendency of metal atoms to evolve into an isotropic 3D crystal lattice. Hence, to generate an anisotropic structure, it is essential to introduce appropriate confinement to suppress the natural tendency for isotropic crystal growth.^[24] Recently, we have developed a one-step method for the fabrication of freestanding, sub-nanometer thick Au nanosheets (Au nanoseaweeds, AuNSWs) by using methyl orange (MO) as a confining agent.^[25] The reaction system in the absence of MO yields quasi-spherical Au nanoparticles, confirming that MO is capable of inducing the growth of 2D gold nanostructures. The results of simulation and control experiments suggest possible roles of MO in regulating the formation of <111> oriented AuNSWs: confining template provided by the 2D planar stacking and preferential adsorption of MO on Au {111} to restrict the growth along the <111> direction. We suggest that the formation of AuNSWs involves the initial growth of small Au nanoflakes as confined by MO and their subsequent coalescence via oriented attachment at side facets. Bromide ions have been documented to have facet-blocking effects on the growth of gold nanocrystals via preferential adsorption on Au (100).^[26] Thus we envisaged that, introduction of bromide ions to our MO-based synthesis might lead the nascent Au nanoflakes to interact via basal facets, resulting in an evolution from 2D sub-nanometer thick nanosheets to quasi-2D nanoplates. Indeed, a reaction system composed of HAuCl₄, sodium citrate (SC), MO, and FeBr₃, yielded (truncated) triangular AuNPLs (**Figure 1**).

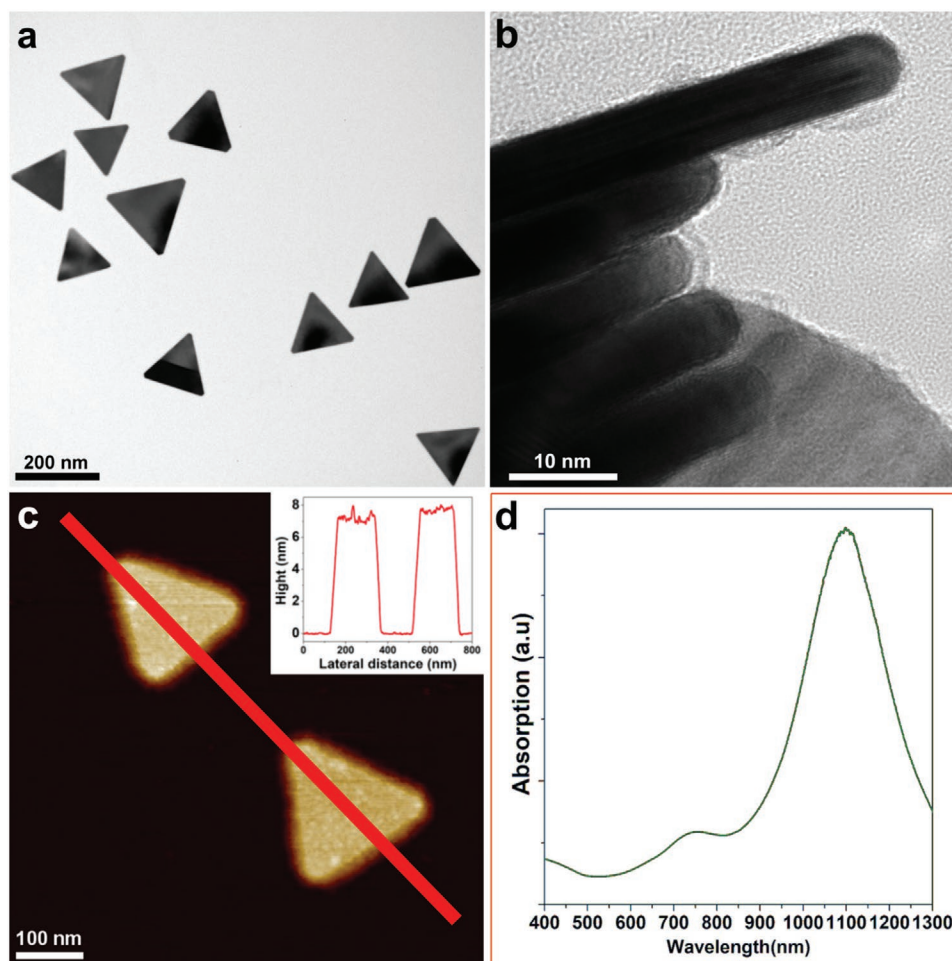


Figure 1. Characterization of AuNPLs (average edge length: 148 nm): a) low-magnification TEM image (histograms of nanoplate edge lengths and thicknesses are shown in Supporting Information); b) TEM image of a stack of AuNPLs viewed side-on; c) AFM image of two AuNPLs on mica (inset shows the height profile along the red line.); d) UV-vis-NIR spectrum.

In a typical synthesis of AuNPLs, FeBr_3 aqueous solution (see Experimental Section), HAuCl_4 aqueous solution (1 mL, 5 mM) and SC aqueous solution (freshly prepared, 0.5 mL, 100 mM) were sequentially added into an aqueous solution of MO (3 mL, 0.28 mM). The resultant reaction mixture was kept undisturbed at 20 °C for 12 h. Reaction products were collected by centrifugation and washed with Milli-Q water until the supernatant was colorless. The pellet was redispersed in Milli-Q water for characterization.

Figure 1a shows a representative transmission electron microscope (TEM) image of the as-prepared nanostructures. It demonstrates that, truncated triangular AuNPLs with an edge length of (148 ± 28) nm have been obtained at a remarkably high nanoplate yield of >95% (defined as the number fraction of AuNPLs compared with other morphologies, such as spherical nanoparticles. Figure S1, Supporting Information shows the histogram and Scheme S1, Supporting Information shows the edge-length definition). It is important to note that previous studies have revealed that almost all colloidal syntheses of triangular gold or silver nanoplates tend to produce hexagonal nanoplates (or significantly truncated triangular nanoplates),^[2] which were also observed in a small fraction in our sample (Figure S2, Supporting Information). Here, the formation of stacks of AuNPLs

lying perpendicular to the electron beam direction allowed a direct plate thickness measurement by TEM (Figure 1b). The thickness was determined to be (6.3 ± 0.3) nm (excluding an organic capping layer, which is observable in Figure 1b). AFM analysis (Figure 1c and Figure S2, Supporting Information) of AuNPLs reveals that the top and bottom faces are atomically flat, with a thickness of (7.5 ± 0.4) nm (including the capping layer). The high shape purity of the product is corroborated by the UV-vis spectrum (Figure 1d), where the absence of a peak at ≈ 520 nm suggests a spectrally undetectable yield of isotropic nanostructures.^[15] The AuNPLs display distinct local surface plasmon resonance (LSPR) features at 1100 and 750 nm, which can be assigned to in-plane dipolar and quadrupolar plasmon resonances, respectively.^[9] It is noteworthy that, the peak corresponding to in-plane quadrupole plasmon resonance has only been distinguishable in colloidal solutions of AuNPLs that have a high homogeneity and nanoplate yield.^[2,9]

2.2. Crystalline Structure of AuNPLs

We further investigated the crystalline structure of our AuNPLs. Distinct Moiré fringes were observed at the overlapped portions

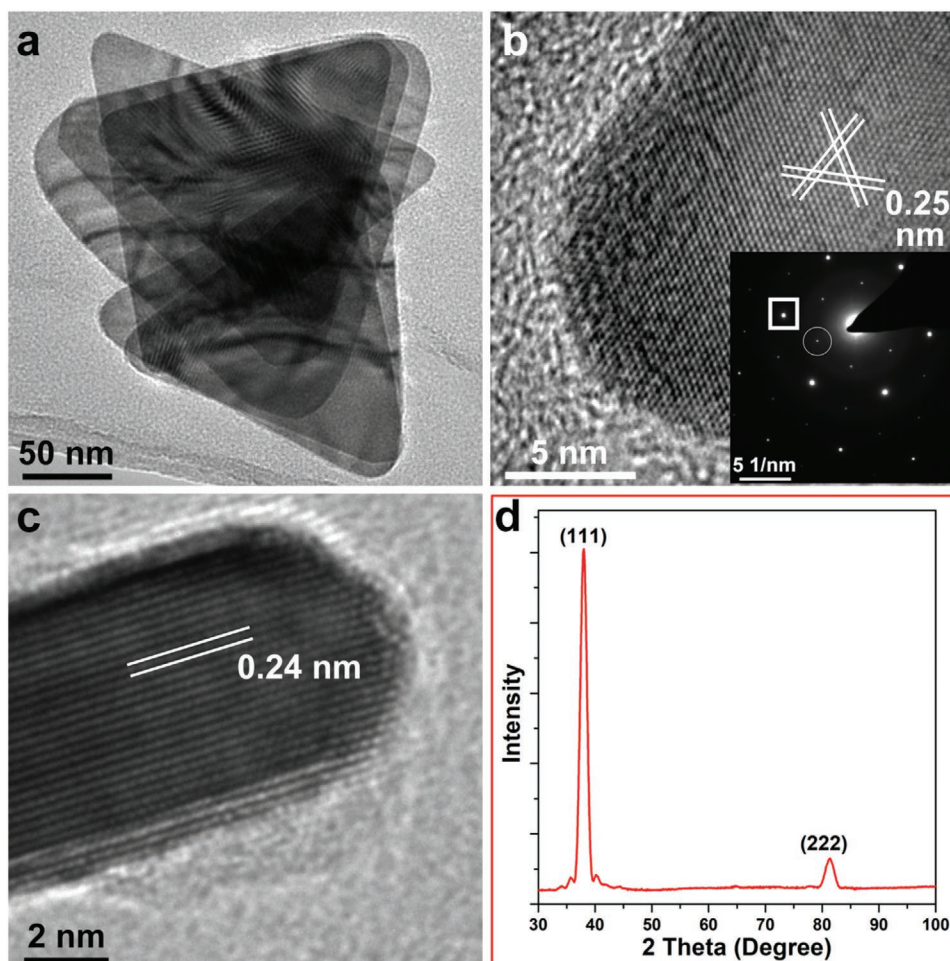


Figure 2. Crystalline structure of AuNPLs: a) high-magnification TEM image, showing Moiré fringes at the overlapped portions; b) HRTEM image of the top face of an Au nanoplate. The spacing between each set of white parallel lines is measured to be ≈ 0.25 nm, corresponding to the $1/3\{422\}$ lattice spacing of fcc-gold. Inset shows the SAED pattern down the $\langle 111 \rangle$ zone axis: strong spots (boxed) are indexed to the allowed $\{220\}$ Bragg reflections (corresponding to a lattice spacing of 0.144 nm); weak spots (circled) are indexed to the forbidden $1/3\{422\}$ reflections (corresponding to a lattice spacing of 0.250 nm); c) HRTEM image of the side face of an individual AuNPL. The spacing between the white lines is ≈ 0.24 nm, corresponding to the $\{111\}$ interplanar spacing of fcc-Au; d) Indexed XRD pattern of AuNPLs over a 2θ range from 30° to 100° confirming the purity and preferential $\langle 111 \rangle$ orientation of AuNPLs.

of our AuNPLs in bright-field TEM images (Figure 2a), indicating their single-crystalline property and uniform thickness.^[27] As shown in the high-resolution TEM (HRTEM) image (Figure 2b), an individual AuNPL manifests a sixfold symmetric structure. The lattice spacing was measured to be 0.25 nm, consistent with that of $1/3\{422\}$ planes in fcc-Au. Two sets of spots with sixfold symmetry were observed in the SAED pattern taken along the $\langle 111 \rangle$ zone axis (inset in Figure 2b). The strong spots correspond to the lattice spacing of 0.144 nm, indexed to the allowed $\{220\}$ Bragg reflection. The weak spots (circled) correspond to the lattice spacing of 0.250 nm, indexed to the forbidden $1/3\{422\}$ reflections. Notably, the presence of this forbidden reflection has been demonstrated to be only observable for atomically flat, ultrathin gold (or silver),^[28,29] and is attributable to stacking faults in a nanoplate sample.^[30] The absence of other reflections in the SAED pattern also implies the single-crystal nature of the AuNPLs. The HRTEM image of the side face of AuNPLs (Figure 2c) shows a lattice spacing

of ≈ 0.235 nm, consistent with the $\{111\}$ interplanar spacing of fcc-Au. The expected stacking faults in the $\{111\}$ layers are more obvious in lower-magnification bright-field TEM image (Figure 1b). The HRTEM and SAED results suggest that the AuNPLs are $\langle 111 \rangle$ oriented single crystals, in accordance with the XRD pattern (Figure 2d), which exhibits only $\{111\}$ peaks. Pendellösung fringes observed symmetrically around the $\{111\}$ peak indicate our AuNPLs are highly perfect crystals.^[31]

2.3. Evaporative Self-Assembly of AuNPLs

Ordered assemblies of nanostructures have shown tremendous potential for construction of complex functional architectures, owing to the unique collective properties that arise from coupling between the individual building blocks.^[32,33] Assemblies of anisotropic nanocrystals are of particular interest. They display diverse assembly patterns caused by the reduced structural

symmetry, and intriguing features that depend on the orientation of assembly, spatial configuration, and the degree of order.^[34] Several colloidal approaches have been exploited to regulate the assemblies of anisotropic nanocrystals, for example, block copolymer-mediated self-assembly,^[35] Langmuir–Blodgett assembly,^[36] and interfacial self-assembly.^[37] Droplet evaporation has been recognized as a simple yet versatile non-lithographic technique to form regular assembly of nanocrystals.^[7,38] Typically, when a droplet containing non-volatile solutes dries on a surface, the solute tends to be carried by the outward flow of the solvent to the pinned edge of the droplet, yielding a

ring-like pattern of solutes. This phenomenon is often termed the “coffee ring” effect and has been explained by considering the granules to be advected to the pinned contact line as the drop height reduces due to evaporation.^[39] A study on the evaporation-induced self-assembly of silver nanoplates deposited in this way has demonstrated that high monodispersity and shape purity are key contributors to the long-range ordering of formed assemblies.^[40] In our work, AuNPLs assemble into arrays with stacking orientations parallel or perpendicular to a substrate upon evaporation (**Figure 3**), including (in order of increasing concentration): I) short-column arrangements (columns

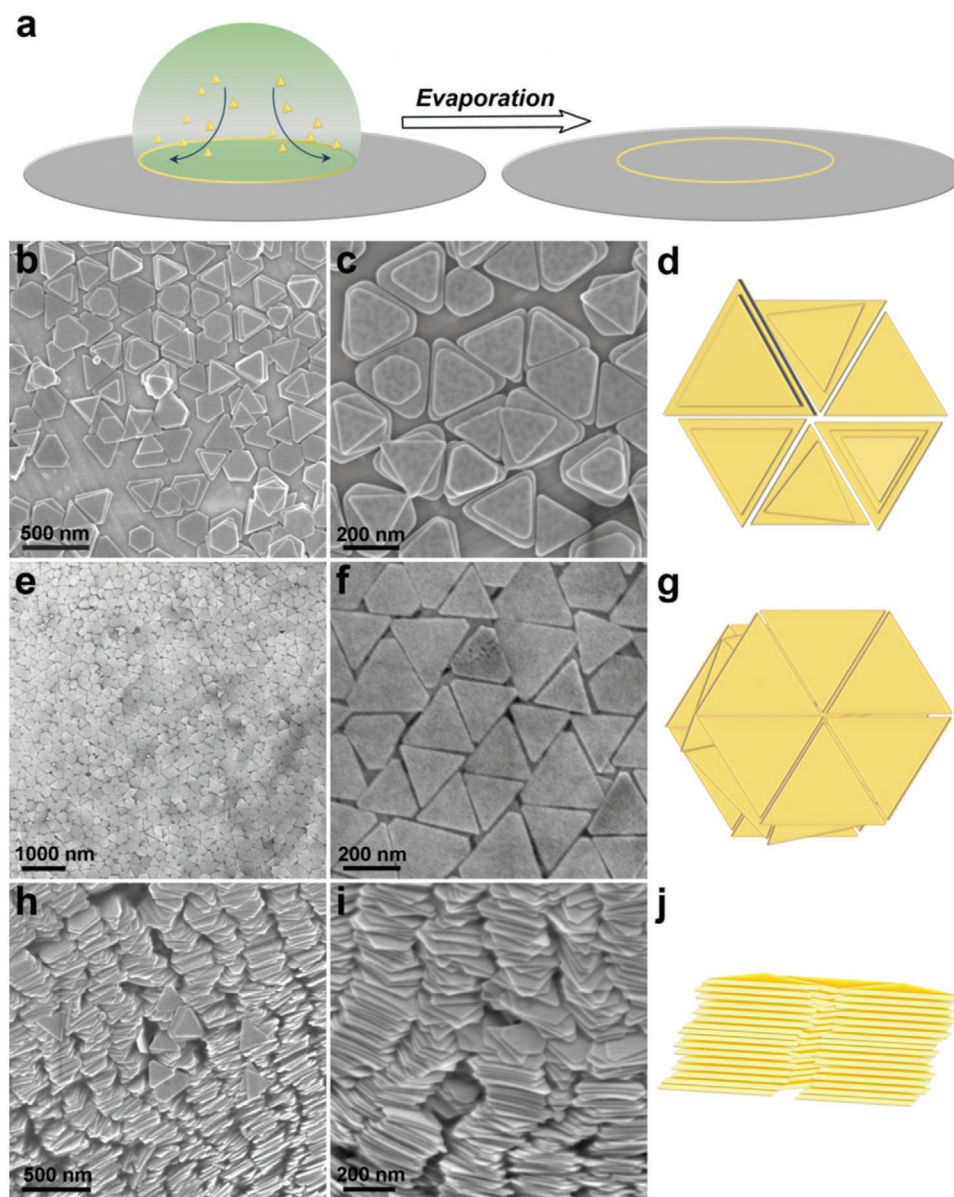


Figure 3. a) Schematic illustration of the evaporation-induced “coffee ring” with organized AuNPLs. Arrows in the droplet point out the direction of convective flows. Self-assembly of AuNPLs at the concentration of $5 \mu\text{g mL}^{-1}$: b) low- and c) high-magnification SEM images, demonstrating the short-column arrangements (columns oriented perpendicular to the substrate), schematically shown in (d). Self-assembly of AuNPLs at the concentration of $50 \mu\text{g mL}^{-1}$: e) low- and f) high-magnification SEM images, demonstrating the multilayer lamellar arrangements, schematically shown in (g). Self-assembly of AuNPLs at the concentration of $500 \mu\text{g mL}^{-1}$: h) low- and i) high-magnification SEM images, demonstrating the long-column arrangements (columns oriented parallel to the substrate), schematically shown in (j).

oriented perpendicular to the substrate), II) multilayer lamellar arrangements, and III) long-column arrangements (columns oriented parallel to the substrate).

To form evaporative self-assembly of AuNPLs, 10 μL of a dispersion of AuNPLs (5, 50, or 500 $\mu\text{g mL}^{-1}$) was drop-cast onto an SEM stub for evaporation. Assuming the drop shape to be a hemispherical cap and using the measured contact line diameter of 2.9 mm (Scheme S2, Supporting Information), the contact angle is $\approx 106^\circ$. The arrangements of the assembled AuNPLs vary significantly depending on the initial concentration. Drops with 5 and 50 $\mu\text{g mL}^{-1}$ dispersion show nanoplates with the flat basal face in contact with the substrate and with the edges of the neighboring nanoplates aligning with each other so as to facilitate dense coverage. The 5 $\mu\text{g mL}^{-1}$ sample contains one- to two-layer stacks with some empty spaces. The 50 $\mu\text{g mL}^{-1}$ sample shows a multilayer stack with almost perfect coverage. The conflict between full coverage and particle size polydispersity is resolved via the formation of rhombus mesoshapes by similarly sized nanoplates and using predominantly smaller particles to fill any void. The particle arrangement from the 500 $\mu\text{g mL}^{-1}$ dispersion was qualitatively different, with the nanoplates deposited as wavy columns formed by stacks of nanoplates with the side edges in contact with the substrate. The volume fraction of a droplet occupied by the nanoplates at even the highest concentration explored is small enough to justify ignoring any effect of the nanoplate on the solvent flow field and we only consider the effect of the solvent flow field on the particles in understanding the arrangement of the particles in these experiments. Noting that in our experiments we find particle depositions at the rim of the initial droplet, we ignore additional convective flows.^[41,42] Because the flat substrate introduces a no-slip boundary condition, close to the substrate the local flow-field approximates to a simple shear flow with the velocity oriented along the radial direction and the shear gradient direction is along the normal to the substrate.^[43] Isolated plate-like particles align with their surface normal along the shear gradient direction in a simple shear flow.^[44] As the concentration of nanoplates increase, hydrodynamic simulations show face-to-face clustering of such particles to lower the hydrodynamic drag.^[45] Particles in such a cluster behave like a single rigid dynamic object. At even higher density, the number of plates in a cluster will become large, leading to an effective rod-like dynamical object. Elongated objects typically align their long axis along the flow. Note that in this scenario, the long axis of the dynamical composite object is the same as

the surface normal of the plates. Thus, with increasing concentration of nanoplates, the surface normal of the nanoplates shift from the shear gradient to the flow direction, responsible for the observed change in the nanoplate orientation (Figure 3). This study shows that simple evaporative deposition from a droplet provides the ability to generate arrays of nanoplates with stacking orientations parallel or perpendicular to a substrate, offering a route to produce patterns that have distinct collective plasmonic modes and potential for uses in photonic applications.

2.4. Formation Mechanism of Single-Crystalline AuNPLs

Based on our recent work on the synthesis of sub-nanometer thick 2D Au nanosheets,^[25] we ascribe the successful fabrication of single-crystalline gold AuNPLs in the present study to the combined introduction of methyl orange and bromide ions as structure-directing agents. This is supported by a series of control experiments, with reaction conditions and results presented in Table 1.

Taking these results together, we have identified the roles of MO and bromide ions in the formation of AuNPLs. We suggest that MO directs the formation of nascent 2D nanoflakes by providing the 2D planar stacking and preferential adsorption of MO on Au {111} to restrict the growth along the $\langle 111 \rangle$ direction. In the absence of bromide ions, AuNSWs were formed via the initial growth of small Au nanoflakes confined by MO and their subsequent coalescence via oriented attachment at side facets.^[25] Previous experiments and molecular dynamics simulation have revealed that bromide ions have a stronger adsorption on (100) than (111) facets, hence exerting facet-blocking effects on the growth of gold nanocrystals.^[26,46] A low concentration of bromide ions (0.21 mM) provides an insufficient surface passivation of Au (100) facets, as a result, nascent nanoflakes could attach at both side and basal facets, followed by aggregation and reconstruction to give rise to hierarchical superstructures composed of nanosheets (Figure S5, Supporting Information). Increased concentration of bromide ions provides more complete passivation of Au (100) facets, so that the attachment only takes place at the basal facets to produce quasi-2D nanoplates.^[47] The thickness of AuNPLs is then determined by the number of Au nanoflakes that undergo basal attachment along the vertical direction. Most importantly, we have clearly demonstrated empirical thickness control of AuNPLs, which has been hitherto elusive.

Table 1. Summary of reactants and structures of resultant products.

Reagent(s) in addition to HAuCl_4 and SC	Structure of products
None	Quasi-spherical nanoparticles ^[25]
MO	Seaweed-like 2D Au nanosheets of sub-nanometer thickness ^[25]
FeBr_3	Twinned nanoparticles (Figure S4, Supporting Information)
FeBr_3 (0.21 mM) and MO	Hierarchical superstructures consisting of nanosheets (Figure S5, Supporting Information)
FeBr_3 (in a concentration range of 0.63–3.78 mM) and MO	AuNPLs of thickness that increases with FeBr_3 concentration (Figures 1a and 4a–d)
NaBr (1.89 mM) and MO	AuNPLs (Figure 4k)
FeNO_3 and MO	Aggregations of nanoflakes and nanoparticles (Figure S6, Supporting Information)

2.5. Thickness Control and Edge-Length Tunability

The thickness of our AuNPLs can be easily tuned from ≈ 7 to ≈ 20 nm (as measured by AFM), by increasing the concentration of FeBr_3 from 0.63 to 3.75 mM, accompanied by an alteration of average edge length from ≈ 150 nm to 2.18 μm (Figure 4a–i, see Table S1, Supporting Information for details). Micro-sized nanoplates (average edge lengths of 1.12 or 2.18 μm) also exhibit single crystallinity, with atomically flat surfaces of a {111} phase (Figures S7 and S8, Supporting Information).

Aspect ratio (AR, defined as the edge length/thickness) is an important structural parameter governing the physical properties of AuNPLs, and has been investigated here as a function of the concentration of FeBr_3 . (Note that AR values shown in Figure 4j were based on the thickness excluding the capping organic layer, assumed to be 1.2 nm according to Figure 1, so as to align with the subsequent study of plasmonic properties.) The data in Figure 4j indicate two regimes of AR variation. In the first regime, the increase of FeBr_3 concentration from

0.63 to 1.42 mM leads the AR value to gently increase from 23.3 to 25.9, with the coefficient of variation (CV) of edge length in the range of 12.5–18.9% (Figure S12, Supporting Information). In the second regime when the FeBr_3 concentration is increased from 1.42 to 3.78 mM, AR increases sharply from 26.5 to well over 100 and shows a much larger CV of edge length ($\approx 29\%$). The introduction of increasing levels of bromide ions can considerably slow down the reduction process generating Au atoms (reduction potential: $\text{AuBr}_4^-/\text{Au}^0$: +0.854 V, NHE; $\text{AuCl}_4^-/\text{Au}^0$: +1.002 V,^[48] NHE; NHE, normal hydrogen electrode), inducing an autocatalytic surface reduction,^[49] which may contribute to the drastic increase of AR and CV of edge length in this regime.

In addition, the formation of AuNPLs having the same edge length (average edge length: 150 nm, Figure S13, Supporting Information shows the histogram of edge lengths.) as those shown in Figure 1, coupled with different thickness was realized by changing the counterions from Fe^{3+} to Na^+ . As can be seen in Figure 4k, the reaction system composed of MO, NaBr,

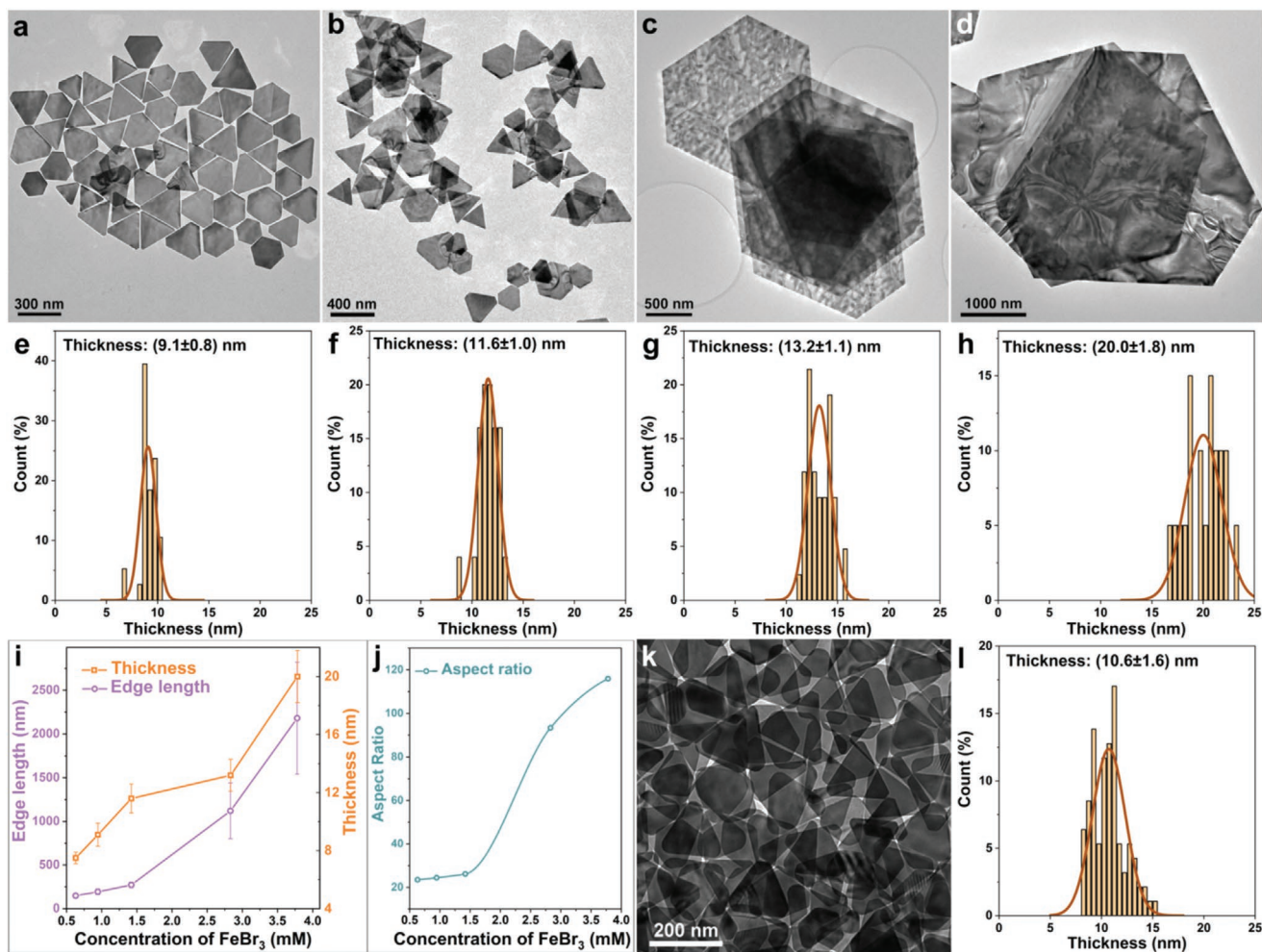


Figure 4. The edge length and thickness of AuNPLs can be tuned by adjusting the concentration of FeBr_3 . TEM images of AuNPLs with average length of a) 193 nm, b) 272 nm, c) 1.12 μm , and d) 2.28 μm . Histogram of thicknesses for AuNPLs with an average edge length of e) 193 nm, f) 272 nm, g) 1.12 μm , and h) 2.28 μm . Histograms of edge lengths of these AuNPLs are shown in Figures S9–S11, Supporting Information, f) 272 nm, g) 1.12 μm , and h) 2.28 μm . i) Plot showing the edge length and thickness (determined by AFM) of AuNPLs versus concentration of FeBr_3 . j) Plot showing the aspect ratio versus the concentration of FeBr_3 . Synthesis using NaBr yields AuNPLs: k) TEM image and l) histogram of thicknesses.

Table 2. Summary of structure parameters of AuNPLs.

Sample	Average edge length [nm]	Thickness [nm]	Aspect ratio
AuNPL I	150	9.4	16.0
AuNPL II	148	6.3	23.5
AuNPL III	193	7.9	24.4
AuNPL IV	272	10.4	26.2

Thickness presented in Table 2 represents the average thickness measured by AFM excluding the capping organic layer (assumed to be 1.2 nm according to Figure 1). AuNPL I: synthesized with NaBr (1.89 mM); AuNPL II: synthesized with FeBr₃ (0.63 mM); AuNPL III: synthesized with FeBr₃ (0.95 mM); AuNPL IV: synthesized with FeBr₃ (1.42 mM).

HAuCl₄, and SC produces (truncated) triangular AuNPLs at a high yield (>92%), with the thickness determined by AFM to be 10.6 ± 1.6 nm (Figure 4l, see Table 2 for details in structure parameters). These AuNPLs exhibit single crystallinity with {111} basal domains (see HRTEM image and SAED pattern in Figure S14, Supporting Information). This thickness modulation induced by altering the counterions is attributable to the change of ionic strengths in the reaction system, which may alter the way in which the small building blocks interact with each other in the vertical direction. Although a complete understanding of the mechanism for the formation and dimension control of our AuNPLs needs further investigation and is beyond the scope of this work, the demonstration here of concurrent control of thickness and edge length has allowed the production of AuNPLs with an adjustable aspect ratio, that would allow manipulation of optical properties.

2.6. Modulation of Optical Properties

The optical properties of metal nanoplates are dictated by several architectural parameters including nanoplate dimension and more specifically aspect ratio. Several groups reported experimental results regarding the effect of edge length on the plasmonic properties of metal (Au or Ag) nanoplates. For example, spectra of Ag nanoplates with varying different edge lengths, displayed red-shifts of the in-plane dipolar resonance with an increase in edge length.^[50] Similarly, Millstone et al. tuned the edge length of AuNPLs between 100 and 300 nm while thickness or crystallinity were kept constant. They observed a linear correlation between the peak positions of the in-plane quadrupolar plasmon resonance and edge length.^[51] Since tailoring thickness has been difficult to realize, the edge length has been recognized as the responsible factor for these reported spectral shifts. It has also been theoretically pointed out that the aspect ratio actually plays the determining role.^[1] The ability to adjust aspect ratio, demonstrated here, provides a possibility for developing an in-depth understanding of the structure–property relationship for such nanostructures. It can be seen in Figure 5a, the spectra of AuNPLs with AR varying from 16.1 to 25.9 show two SPR peaks, 693–800 and 1035–1205 nm, which can be assigned to in-plane dipolar and quadrupolar LSPR, respectively. The high crystallinity of our AuNPLs contributes to the well-defined resonances, which

allows us to perform spatially resolved scanning TEM-electron energy loss (STEM-EEL) spectrum imaging on an individual nanoplate (Figure 5c,d). The results (from the sample with an AR of 24.4) reveal that the maximum electric-field enhancement occurs at nanoplate corners for the dipolar mode (1.61 eV, i.e., 770 nm), while it lies along nanoplate edges for the quadrupolar mode (1.13 eV, i.e., 1097 nm). This spatial distribution is consistent with the reported results of discrete dipole approximation (DDA) simulation on Ag nanoplates.^[52] Both of these two peaks display a red-shift as the aspect ratio is increased. Notably, AuNPLs with aspect ratios of 16.0 and 23.5 have nearly identical average lengths (150 and 148 nm, respectively) and different thicknesses (9.4 and 6.3 nm; see Table 2 for structure parameters), while the LSPR peaks are significantly red-shifted for the nanoplates of higher AR, that is, AuNPLs with similar average lengths show red-shifts, when they have smaller thickness (6.3 nm compared with 9.4 nm). This suggests that the aspect ratio is indeed the dominant factor determining the wavelength of the LSPRs. Figure 5b shows the plot of peak wavelength of both the dipolar and quadrupolar LSPRs as a function of aspect ratio, suggesting the peak position for both modes exhibited more pronounced red-shifts at higher aspect ratios (in the range of 23.5–26.2). For AuNPLs with micro-scale edge lengths, the UV–vis spectrum showed a broad extinction in the region of 500–1300 nm, with the extinction enhanced at longer wavelength (Figure 5e). The absence of a distinct peak is attributed to delocalized plasmon modes, that is, surface plasmon polaritons, at the micro-meter scale. Single crystallinity and atomic flatness, coupled with a thickness (≈20 nm) smaller than the skin depth of gold collectively cause damping of the near-field enhancement and facilitate light propagation along the edges.^[53] As a result, AuNPLs in a dark-field light microscopy image show darkness on their flat surfaces and significant scattering from edges of the plates (Figure 5f).

2.7. Photothermal Cell Ablation

The well-defined and tunable optical properties provide exciting opportunities for developing our AuNPLs toward plasmonic-based applications. For instance, the two SPR peaks of our AuNPLs are located in 650–950 nm (NIR I window) and 1000–1400 nm (NIR II window), respectively.^[54] This motivated us to explore their cancer therapeutic potential as photothermal agents (PTAs). Photothermal cancer therapy utilizes the efficient conversion of light into heat to preferentially kill cancer cells through localized temperature increases.^[55] Ideal therapeutic PTAs should possess low toxicity and high optical absorption in the NIR biological transparency windows (NIR I: 650–900 nm and NIR II: 1000–1400 nm).^[54] Compared with the widely studied NIR I window, the NIR II window offers several advantages, such as low autofluorescence, increased penetration depth, and larger value of maximum permissible exposure of skin.^[56–58] So far, reports of PTAs with a plasmonic peak in NIR II window have been scant. Thus, distinct SPR peaks in both the NIR I and NIR II windows, alongside a preparation method free of CTA surfactant mean that our AuNPLs may be effective and safe PTAs.

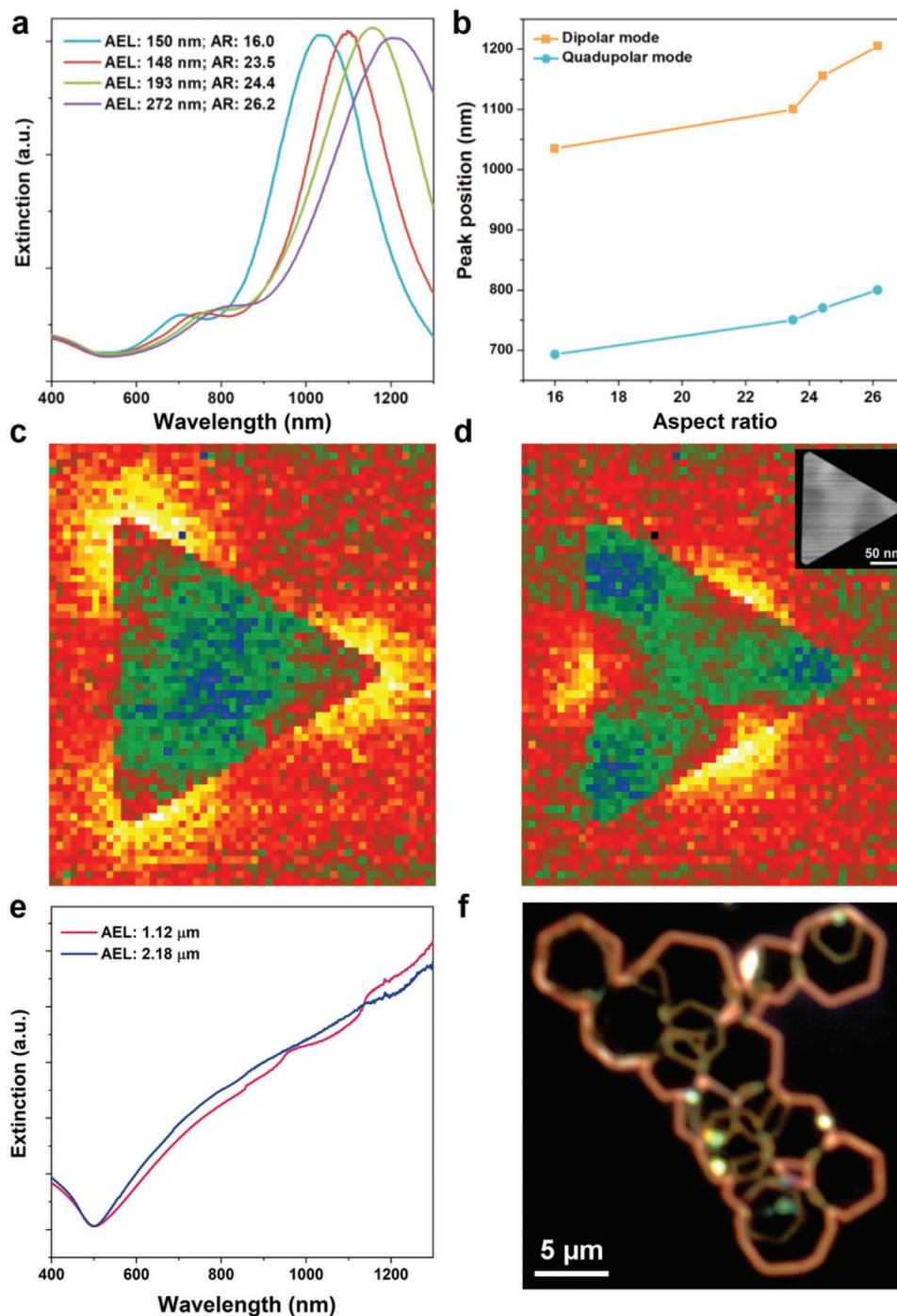


Figure 5. Adjustable optical properties of AuNPLs: a) UV-vis spectra of AuNPLs of varying average edge lengths (AELs) and aspect ratios (ARs). Table 2 shows a summary of structure parameters of these AuNPL samples. b) Plot of LSPR (in-plane dipole and quadrupole mode) positions as a function of AR of AuNPLs. STEM/EELS spectrum images collected from an individual nanoplate of AR 24.4: c) dipolar mode (from 1.1 to 1.2 eV); d) quadrupolar mode (from 1.6 to 1.7 eV); an STEM dark-field image is shown in the inset in (d) with a scale bar of 50 nm. e) UV-vis spectra of AuNPLs with AELs of 1.12 and 2.18 μm. f) Dark-field light microscopy image of AuNPLs with an AEL of 2.18 μm.

We have investigated the cellular uptake of AuNPLs by human colorectal cancer cells (SW480 cells), using light microscopy and TEM imaging. In the bright-field (BF) light microscopy images (Figure 6a,b), cells treated with AuNPLs exhibit their normal morphology, which indicates good

biocompatibility of AuNPLs. Figure 6c,d show the dark-field (DF) microscopy images of SW480 cells without treatment and after incubation with AuNPLs at 37 °C for 4 h, respectively. The cells were fixed with paraformaldehyde/DPBS and rinsed with DPBS for several times to remove excess AuNPLs prior to

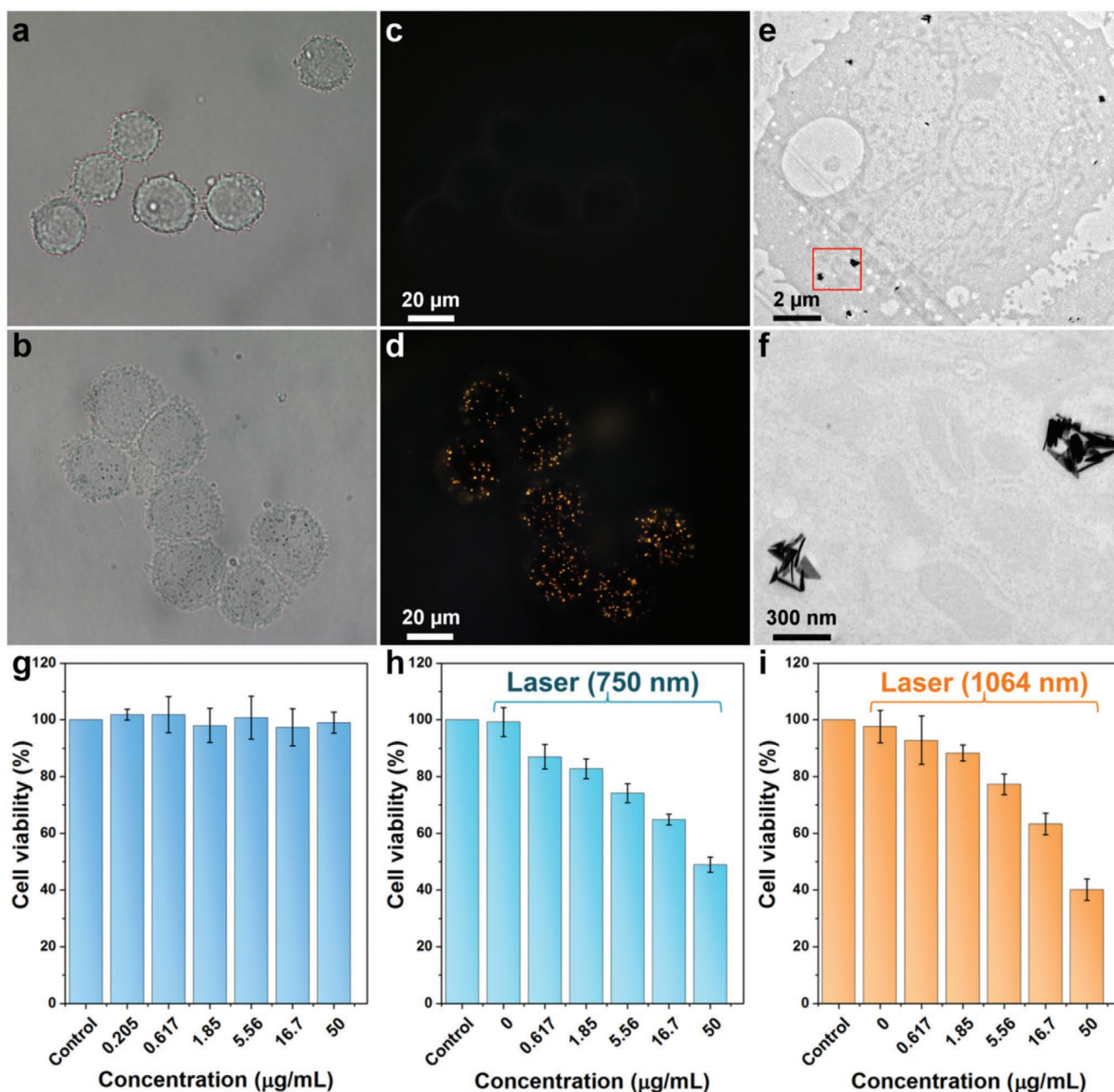


Figure 6. Bright-field microscopy image of a) untreated SW480 cells and b) SW480 cells incubated with AuNPLs ($50 \mu\text{g mL}^{-1}$); DF microscopy image of c) untreated SW480 cells and d) SW480 cells incubated with AuNPLs ($50 \mu\text{g mL}^{-1}$). e) Low-magnification TEM image of a section of a fixed SW480 cell after incubation with AuNPLs, f) high-magnification TEM image showing an enlarged view corresponding to the box in (e). g) In vitro SW480 cell viability after treatments with different dosages of AuNPLs. Results are shown as mean \pm SD as determined using CCK-8 assays. In vitro viability of SW480 cells post incubation with varying dosages of AuNPLs and irradiation with the 7 ns pulse laser, at a wavelength of (j) 750 nm, at a radiant exposure of 26 mJ cm^{-2} per pulse for 60 s and i) 1064 nm, at a radiant exposure of 5 mJ cm^{-2} per pulse for 60 s. Cells that were cultured in the absence of AuNPLs without laser exposure were used as a control group. Results are shown as mean \pm SD.

imaging. The untreated SW480 cells showed no scattering signals. In contrast, treated cells displayed orange-pink scattering signals arising from the strong optical scattering of AuNPLs in the NIR region. Furthermore, these scattering signals were observed to be located in the cytoplasm with a lack of signal in the nuclear regions, rather than being randomly co-located with cells, suggesting the cellular internalization of the AuNPLs

instead of simple attachment to the cell surface. In order to reveal the subcellular distribution of the AuNPLs, SW480 cells treated with AuNPLs were subjected to fixation, resin embedding, microtome sectioning, and TEM imaging. As can be seen in Figure 6e,f, AuNPLs were internalized by the cells and distributed mainly in endosomes, suggesting internalization via an endocytic pathway. Next we assessed the cytotoxicity of AuNPLs

using SW480 cells with CCK-8 (Cell Count Kit 8) assay. After 48 h incubation with AuNPLs at varying doses, SW480 cells showed a viability above 90% at each examined concentration (Figure 6g). These results suggest our AuNPLs have very low cytotoxic effects on SW480 cells. We then evaluated the applicability of AuNPLs for photothermal cell ablation with a NIR laser at 750 and 1064 nm (Figure 6h,i), using laser exposures substantially below the safe exposure limits for clinical standards.^[59] In the absence of AuNPLs, the viability of SW480 cells is $\approx 100\%$ post irradiation at 750 or 1064 nm, demonstrating that the laser exposure does not cause cell ablation, without the use of AuNPLs. With the introduction of AuNPLs, the phototoxicity is observed to increase with the increase in AuNPL concentration. The cell viability decreased to 48.9% after laser exposure at 750 nm, and to 40.1% after the laser exposure at 1064 nm for cells incubated with AuNPLs at $50 \mu\text{g mL}^{-1}$. These results substantiate that, in combination with laser illumination, our AuNPLs are able to induce photothermal cell ablation in both the NIR I and NIR II biological windows, outperforming most Au-based nanoagents reported, particularly with NIR II irradiation (see Tables S2 and S3, Supporting Information for the comparison).

3. Conclusion

We present a novel and robust approach to the one-step, high-yield synthesis of biocompatible AuNPLs with tunable thickness, lateral size, and plasmonic properties. Our AuNPLs showed ordered self-assembly over mesoscale, owing to high shape uniformity. In addition to extending the controllability of anisotropic nanostructures, access to this tailorable class of well-defined nanostructures will encourage diverse plasmonic investigations. These AuNPLs could function as building blocks in the superstructural assembly of optical metamaterials. Their quasi-2D shape facilitates the formation of assemblies exhibiting unique packing symmetries, and the synthesis route avoiding CTA-halide surfactants delivers good biocompatibility as well as easy bio-functionalization. These attributes are beneficial for studies on the fundamental plasmonic coupling, the engineering of plasmonic devices, and plasmon-based (bio-) sensing, imaging and therapeutic functions. The approach developed here, based on the cooperative utilization of two structure-directing agents that have preferential adsorption onto different crystalline facets of Au, can be expanded to other compositions as a universal method for fabricating anisotropic nanostructures. Thus, our work provides synthetic methodologies for designing and constructing more sophisticated nanoarchitectures with physicochemical characteristics optimized for specific applications.

4. Experiment Section

Chemicals and Materials: Gold (III) chloride trihydrate and iron(III) nitrate nonahydrate (254 223) were purchased from Sigma-Aldrich (520 918). Trisodium citrate, anhydrous (45 556), iron(III) bromide, anhydrous (11 387 408), sodium bromide (A10552), and methyl orange (17 874) were purchased from Alfa Aesar. 37% Hydrochloric acid (UN1789) and 70% nitric acid (UN2031) were purchased from Fisher

Scientific. All chemicals were used without further purification. Milli-Q water ($18.2 \text{ M}\Omega \text{ cm}$ at $25 \text{ }^\circ\text{C}$) was used in all the experiments.

Characterization: UV-vis spectra were recorded with a Perkin Elmer UV/VIS/NIR Lambda 19 spectrophotometer. XRD pattern was obtained using a Bruker D8 X-ray diffractometer with Cu $K\alpha$ source and an X'cellerator detector. A continuous scan over a 2θ range from 30° to 100° was performed with an acquisition time of 1 h per sample at a step size of 0.05° . The sample for XRD measurement was prepared by depositing and drying AuNPL dispersion directly on low-background Si sample holders. AFM height measurements of AuNPLs were carried out on a Dimension FastScan Bio AFM (Bruker, Billerica MA), using tapping mode at room temperature in air with FastScan-A cantilever probes (Bruker, Camarillo CA). Analyses of sample heights were performed using Bruker Nanoscope Analysis v1.9. SEM images were obtained using a Hitachi SU8230 at a voltage of 2 kV. Dark-field microscopy imaging of AuNPL sample was conducted using a Nikon Ti-S microscope with a TI-DF dry dark-field condenser, a CFI Plan Fluor $100\times$ oil-coupled objective, as well as an Olympus UC90 camera. Bright-field TEM images, SAED patterns, and STEM/EELS spectrum images were collected using a range of microscopes at the University of Leeds: a Tecnai G2 Spirit TWIN/BioTWIN at an acceleration voltage of 120 kV; a Tecnai F20 TEM/STEM operated at an accelerating voltage of 200 kV and equipped with a field emission gun using an extraction voltage of 4.5 kV; an Oxford Instruments 80 mm² SD detector running Aztec software, and a Gatan Orius CCD camera running Digital Micrograph software; and a FEI Titan3 Themis G2 S/TEM operated at 300 kV equipped with a monochromator (giving an EELS energy resolution of 0.25–0.3 eV measured at a dispersion of 0.01 eV per channel), FEI SuperX EDX detectors, a Gatan Quantum ER 965 imaging filter, and a Gatan OneView CCD camera running GMS 3.1. For preparing the TEM samples, $2 \mu\text{L}$ nanoparticle dispersion (in Milli-Q) was dropped onto a carbon-coated copper grid (Agar Scientific Ltd) and air dried at room temperature. For STEM/EELS analysis, dispersions of nanostructures were directly drop cast onto non-porous, pure silicon, 5 nm thick TEM support films consisting of nine small windows (purchased from EM Resolutions) and left to dry naturally. Individual AuNPLs were selected for the acquisition of EEL spectra with sufficient space between particles so as to avoid plasmonic coupling effects. All EELS data processing was undertaken using Gatan Digital Micrograph software. The EELS data in Figure 5c,d are presented in 3D SI maps where the x - y pixel represents the probe position and the z -pixel value the intensity of the EELS spectrum integrated over a particular energy range (using an energy window of width 0.1 eV). Spectra were acquired with an exposure time of 0.002 s per pixel over a selected area to provide a sufficient signal to noise ratio, whilst minimizing the effects of sample drift, hydrocarbon contamination, and sample damage. The tail of zero-loss peak (ZLP), which forms the background in this low energy loss region was carefully removed using a power law subtraction method. In order to compare the different SI maps and visualize the plasmonic mode of Au nanostructures, the SI maps were normalized to the total electron counts over all selected pixels.

Synthesis of AuNPLs with an Average Length of 148, 193, or 272 nm: FeBr_3 aqueous solution (freshly prepared, 1 mL, certain concentration, see Table S1, Supporting Information), HAuCl_4 aqueous solution (1 mL, 5 mM), and freshly prepared SC aqueous solution (0.5 mL, 100 mM) were sequentially added into MO aqueous solution (3 mL, 0.28 mM) at $20 \text{ }^\circ\text{C}$. The resultant reaction solution was kept undisturbed at this temperature for 12 h. The reaction products were collected by centrifugation ($3000 \times g$ for 10 min) and washed several times with Milli-Q water until the supernatant was colorless. The pellet was then redispersed in Milli-Q water.

Synthesis of AuNPLs with an Average Edge Length of 1.12 or 2.18 μm : FeBr_3 aqueous solution (freshly prepared, 1 mL, at specific concentration, see Table S1, Supporting Information), HAuCl_4 aqueous solution (1 mL, 5 mM), and freshly prepared SC aqueous solution (0.5 mL, 100 mM) were sequentially added into MO aqueous solution (3 mL, 0.28 mM) at $20 \text{ }^\circ\text{C}$. The resultant reaction mixture was kept undisturbed at this temperature for 12 h. The reaction products formed a precipitation at the bottom of the vial. After the removal of the supernatant, the products

were redispersed in Milli-Q water, washed by centrifugation ($1000 \times g$ for 8 min) for several times and then redispersed in Milli-Q water.

Synthesis of AuNPLs with NaBr: NaBr aqueous solution (1 mL, 1.89 mM), HAuCl₄ aqueous solution (1 mL, 5 mM), and freshly prepared SC aqueous solution (0.5 mL, 100 mM) were sequentially added into the MO aqueous solution (3 mL, 0.28 mM) at 20 °C. The resultant reaction solution was kept undisturbed at this temperature for 12 h. The products were collected by centrifugation ($3000 \times g$ for 10 min) and washed several times with Milli-Q water until the supernatant is colorless. The pellet was then redispersed in Milli-Q water.

Evaporative Self-Assembly of AuNPLs: 10 μ L of a dispersion of AuNPL (5, 50, or 500 μ g mL⁻¹) was drop-cast onto a SEM scrub (Aluminum, Agar Scientific) for evaporation.

Syntheses with Interplay of Different Chemical Species: Methods are shown in Supporting Information.

In Vitro Cell Study: Methods are shown in Supporting Information.

Supporting Information

Supporting Information is available from the Wiley Online Library or from the author.

Acknowledgements

The authors would like to thank the following for financial support: Wellcome Trust ISSF Junior Investigator Development Fellowship, MRC (MR/L01629X), MRC-CiC, NIHR (MIC-2016-004), EPSRC (EP/P023266/1), EPSRC (EP/P005241/1), EPSRC Experimental Equipment call M028143/1 for a new transmission electron microscope. Wellcome Trust Equipment Grant (101497/Z/13/Z) for Bruker FastScan Bio AFM. S.Y. thanks the following for suggestions and support: Stuart Micklethwaite and John Harrington (SEM), Martin Fuller (preparation of cell sample for TEM imaging), Dr. Jin Wen (discussion), as well as colleagues from School of Mathematics, University of Leeds. The data presented in this article will be openly available from the University of Leeds data repository <https://doi.org/10.5518/790>.

Conflict of Interest

The authors declare no conflict of interest.

Author Contributions

All authors contributed to the work. S.Y. conceived and performed experiments of synthesis and self-assembly and interpreted results. S.Y., A.P.B., and R.B. collected and analyzed TEM and SAXD data. S.D.C. conducted AFM imaging and analyzed the results. S.Y. collected and analyzed UV-vis spectra and XRD. L.R. assisted in data analysis and performed dark-field imaging of nanoplate sample. Z.A., N.C., and R.B. collected and analyzed the EELS data. L.C., S.D.E., A.F.M., S.Y., K.C., and J.M. conceived cell study. S.Y. performed cell biology experiments with assistance from J.M. in the set-up of photothermal tests. S.D.E., P.L.C., and A.F.M. oversaw this project. S.Y. wrote the manuscript with input from all authors.

Keywords

gold nanoplates, high-yield synthesis, self-assembly, surface plasmon resonance, thickness control

Received: April 21, 2020

Revised: June 12, 2020

Published online:

- [1] I. Pastoriza-Santos, L. M. Liz-Marzan, *J. Mater. Chem.* **2008**, *18*, 1724.
- [2] J. E. Millstone, S. J. Hurst, G. S. Metraux, J. I. Cutler, C. A. Mirkin, *Small* **2009**, *5*, 646.
- [3] L. Scarabelli, M. Coronado-Puchau, J. J. Giner-Casares, J. Langer, L. M. Liz-Marzan, *ACS Nano* **2014**, *8*, 5833.
- [4] M. N. O'Brien, M. R. Jones, K. L. Kohlstedt, G. C. Schatz, C. A. Mirkin, *Nano Lett.* **2015**, *15*, 1012.
- [5] F. Qin, T. Zhao, R. B. Jiang, N. N. Jiang, Q. F. Ruan, J. F. Wang, L. D. Sun, C. H. Yan, H. Q. Lin, *Adv. Opt. Mater.* **2016**, *4*, 76.
- [6] S. Goy-Lopez, J. Juarez, A. Cambon, J. Botana, M. Pereiro, D. Baldomir, P. Taboada, V. Mosquera, *J. Mater. Chem.* **2010**, *20*, 6808.
- [7] D. A. Walker, K. P. Browne, B. Kowalczyk, B. A. Grzybowski, *Angew. Chem., Int. Ed.* **2010**, *49*, 6760.
- [8] K. L. Shuford, M. A. Ratner, G. C. Schatz, *J. Chem. Phys.* **2005**, *123*, 114713.
- [9] J. E. Millstone, S. Park, K. L. Shuford, L. D. Qin, G. C. Schatz, C. A. Mirkin, *J. Am. Chem. Soc.* **2005**, *127*, 5312.
- [10] A. Losquin, L. F. Zagonel, V. Myroshnychenko, B. Rodriguez-Gonzalez, M. Tence, L. Scarabelli, J. Forstner, L. M. Liz-Marzan, F. J. G. de Abajo, O. Stephan, M. Kociak, *Nano Lett.* **2015**, *15*, 1229.
- [11] G. K. Joshi, P. J. McClory, S. Dolai, R. Sardar, *J. Mater. Chem.* **2012**, *22*, 923.
- [12] G. K. Joshi, K. A. Smith, M. A. Johnson, R. Sardar, *J. Phys. Chem. C* **2013**, *117*, 26228.
- [13] Z. X. Tu, G. Guday, M. Adeli, R. Haag, *Adv. Mater.* **2018**, *30*, 1706709.
- [14] R. N. Goyal, A. Aliumar, M. Oyama, *J. Electroanal. Chem.* **2009**, *631*, 58.
- [15] L. Chen, F. Ji, Y. Xu, L. He, Y. F. Mi, F. Bao, B. Q. Sun, X. H. Zhang, Q. Zhang, *Nano Lett.* **2014**, *14*, 7201.
- [16] R. G. Rayavarapu, C. Ungureanu, P. Krystek, T. G. van Leeuwen, S. Manohar, *Langmuir* **2010**, *26*, 5050.
- [17] D. K. Smith, N. R. Miller, B. A. Korgel, *Langmuir* **2009**, *25*, 9518.
- [18] A. M. Alkilany, P. K. Nagaria, C. R. Hexel, T. J. Shaw, C. J. Murphy, M. D. Wyatt, *Small* **2009**, *5*, 701.
- [19] L. Vigderman, P. Manna, E. R. Zubarev, *Angew. Chem., Int. Ed.* **2012**, *51*, 636.
- [20] G. Q. Wang, S. Y. Tao, Y. D. Liu, L. Guo, G. H. Qin, K. Ijiro, M. Maeda, Y. D. Yin, *Chem. Commun.* **2016**, *52*, 398.
- [21] B. Pelaz, V. Grazu, A. Ibarra, C. Magen, P. del Pino, J. M. de la Fuente, *Langmuir* **2012**, *28*, 8965.
- [22] Y. J. Huang, A. R. Ferhan, Y. Gao, A. Dandapat, D. H. Kim, *Nanoscale* **2014**, *6*, 6496.
- [23] W. B. Xin, J. Severino, I. M. De Rosa, D. Yu, J. McKay, P. Y. Ye, X. Q. Yin, J. M. Yang, L. Carlson, S. Kodambaka, *Nano Lett.* **2018**, *18*, 1875.
- [24] X. Q. Huang, S. H. Tang, X. L. Mu, Y. Dai, G. X. Chen, Z. Y. Zhou, F. X. Ruan, Z. L. Yang, N. F. Zheng, *Nat. Nanotechnol.* **2011**, *6*, 28.
- [25] S. J. Ye, A. P. Brown, A. C. Stammers, N. H. Thomson, J. Wen, L. Roach, R. J. Bushby, P. L. Coletta, K. Critchley, S. D. Connell, A. F. Markham, R. Brydson, S. D. Evans, *Adv. Sci.* **2019**, *6*, 1900911.
- [26] J. S. DuChene, W. X. Niu, J. M. Abendroth, Q. Sun, W. B. Zhao, F. W. Huo, W. D. Wei, *Chem. Mater.* **2013**, *25*, 1392.
- [27] T. Soejima, N. Kimizuka, *J. Am. Chem. Soc.* **2009**, *131*, 14407.
- [28] A. I. Kirkland, D. A. Jefferson, D. G. Duff, P. P. Edwards, *Inst. Phys. Conf. Ser.* **1990**, *98*, 375.
- [29] R. C. Jin, Y. W. Cao, C. A. Mirkin, K. L. Kelly, G. C. Schatz, J. G. Zheng, *Science* **2001**, *294*, 1901.
- [30] V. Germain, J. Li, D. Ingert, Z. L. Wang, M. P. Pileni, *J. Phys. Chem. B* **2003**, *107*, 8717.
- [31] N. Kato, A. R. Lang, **1959**, *12*, 787.

- [32] J. Il Park, T. D. Nguyen, G. D. Silveira, J. H. Bahng, S. Srivastava, G. P. Zhao, K. Sun, P. J. Zhang, S. C. Glotzer, N. A. Kotov, *Nat. Commun.* **2014**, *5*, 3593.
- [33] T. Paik, B. T. Diroll, C. R. Kagan, C. B. Murray, *J. Am. Chem. Soc.* **2015**, *137*, 6662.
- [34] T. Ming, X. S. Kou, H. J. Chen, T. Wang, H. L. Tam, K. W. Cheah, J. Y. Chen, J. F. Wang, *Angew. Chem., Int. Ed.* **2008**, *47*, 9685.
- [35] K. Thorkelsson, A. J. Mastroianni, P. Ercius, T. Xu, *Nano Lett.* **2012**, *12*, 498.
- [36] F. Kim, S. Kwan, J. Akana, P. D. Yang, *J. Am. Chem. Soc.* **2001**, *123*, 4360.
- [37] Y. Zhong, Z. X. Wang, R. F. Zhang, F. Bai, H. M. Wu, R. Haddad, H. Y. Fan, *ACS Nano* **2014**, *8*, 827.
- [38] C. J. Brinker, Y. F. Lu, A. Sellinger, H. Y. Fan, *Adv. Mater.* **1999**, *11*, 579.
- [39] R. D. Deegan, O. Bakajin, T. F. Dupont, G. Huber, S. R. Nagel, T. A. Witten, *Nature* **1997**, *389*, 827.
- [40] N. Cathcart, V. Kitaev, *ACS Nano* **2011**, *5*, 7411.
- [41] X. F. Xu, J. B. Luo, *Appl. Phys. Lett.* **2007**, *91*, 124102.
- [42] Z. H. Pan, S. Dash, J. A. Weibel, S. V. Garimella, *Langmuir* **2013**, *29*, 15831.
- [43] H. Hu, R. G. Larson, *Langmuir* **2005**, *21*, 3963.
- [44] I. Bihannic, C. Baravian, J. F. L. Duval, E. Paineau, F. Meneau, P. Levitz, J. P. de Silva, P. Davidson, L. J. Michot, *J. Phys. Chem. B* **2010**, *114*, 16347.
- [45] Q. J. Meng, J. J. L. Higdon, *J. Rheol.* **2008**, *52*, 1.
- [46] S. K. Meena, S. Celiksoy, P. Schafer, A. Henkel, C. Sonnichsen, M. Sulpizi, *Phys. Chem. Chem. Phys.* **2016**, *18*, 13246.
- [47] S. Christodoulou, J. I. Climente, J. Planelles, R. Brescia, M. Prato, B. Martin-Garcia, A. H. Khan, I. Moreels, *Nano Lett.* **2018**, *18*, 6248.
- [48] J. Rodriguez-Fernandez, J. Perez-Juste, P. Mulvaney, L. M. Liz-Marzan, *J. Phys. Chem. B* **2005**, *109*, 14257.
- [49] T. H. Yang, S. Zhou, M. Zhao, Y. N. Xia, *ChemNanoMat* **2020**, *6*, 576.
- [50] I. Pastoriza-Santos, L. M. Liz-Marzan, *Nano Lett.* **2002**, *2*, 903.
- [51] J. E. Millstone, G. S. Metraux, C. A. Mirkin, *Adv. Funct. Mater.* **2006**, *16*, 1209.
- [52] K. L. Kelly, E. Coronado, L. L. Zhao, G. C. Schatz, *J. Phys. Chem. B* **2003**, *107*, 668.
- [53] Z. J. Yan, Y. Bao, U. Manna, R. A. Shah, N. F. Scherer, *Nano Lett.* **2014**, *14*, 2436.
- [54] M. F. Tsai, S. H. G. Chang, F. Y. Cheng, V. Shanmugam, Y. S. Cheng, C. H. Su, C. S. Yeh, *ACS Nano* **2013**, *7*, 5330.
- [55] L. Cheng, C. Wang, L. Z. Feng, K. Yang, Z. Liu, *Chem. Rev.* **2014**, *114*, 10869.
- [56] J. E. Park, M. Kim, J. H. Hwang, J. M. Nam, *Small Methods* **2017**, *1*, 1600032.
- [57] Y. S. Chen, Y. Zhao, S. J. Yoon, S. S. Gambhir, S. Emelianov, *Nat. Nanotechnol.* **2019**, *14*, 465.
- [58] O. B. Knights, J. R. McLaughlan, *Int. J. Mol. Sci.* **2018**, *19*, 3318.
- [59] Laser Institute of America, American National Standard for Safe Use of Lasers, ANSI Z136.1, Laser Institute of America, Orlando, USA **2014**, pp. 1–255.